Ecological Applications, 21(4), 2011, pp. 1120–1137
© 2011 by the Ecological Society of America

Using Lidar and Radar measurements to constrain predictions of forest ecosystem structure and function

Alexander S. Antonarakis,[1] Sassan S. Saatchi,[2] Robin L. Chazdon,[3] and Paul R. Moorcroft[1,4]

[1]*Department of Organismic and Evolutionary Biology, Harvard University, 26 Oxford Street, Cambridge, Massachusetts 02138 USA*
[2]*Jet Propulsion Laboratory, California Institute of Technology, Pasadena, California 91109 USA*
[3]*Department of Ecology and Evolutionary Biology, University of Connecticut, Storrs, Connecticut 06269 USA*

Abstract. Insights into vegetation and aboveground biomass dynamics within terrestrial ecosystems have come almost exclusively from ground-based forest inventories that are limited in their spatial extent. Lidar and synthetic-aperture Radar are promising remote-sensing-based techniques for obtaining comprehensive measurements of forest structure at regional to global scales. In this study we investigate how Lidar-derived forest heights and Radar-derived aboveground biomass can be used to constrain the dynamics of the ED2 terrestrial biosphere model. Four-year simulations initialized with Lidar and Radar structure variables were compared against simulations initialized from forest-inventory data and output from a long-term potential-vegtation simulation. Both height and biomass initializations from Lidar and Radar measurements significantly improved the representation of forest structure within the model, eliminating the bias of too many large trees that arose in the potential-vegtation-initialized simulation. The Lidar and Radar initializations decreased the proportion of larger trees estimated by the potential vegetation by ~20–30%, matching the forest inventory. This resulted in improved predictions of ecosystem-scale carbon fluxes and structural dynamics compared to predictions from the potential-vegtation simulation. The Radar initialization produced biomass values that were 75% closer to the forest inventory, with Lidar initializations producing canopy height values closest to the forest inventory. Net primary production values for the Radar and Lidar initializations were around 6–8% closer to the forest inventory. Correcting the Lidar and Radar initializations for forest composition resulted in improved biomass and basal-area dynamics as well as leaf-area index. Correcting the Lidar and Radar initializations for forest composition and fine-scale structure by combining the remote-sensing measurements with ground-based inventory data further improved predictions, suggesting that further improvements of structural and carbon-flux metrics will also depend on obtaining reliable estimates of forest composition and accurate representation of the fine-scale vertical and horizontal structure of plant canopies.

Key words: biomass; canopy height; ecosystem demography; ecosystem modeling; forest composition; forest structure; La Selva Biological Station, Costa Rica; Lidar; NASA's DESDynI mission; net primary production, NPP; radar; reducing modeling error.

Introduction

Terrestrial ecosystem and biosphere models are essential tools for predicting the expected response of terrestrial ecosystems to changes in climate, CO_2, and other natural and anthropogenic environmental forcings. Optical remote-sensing data sets have been a key source of information on the dynamics of plant canopies at the regional to global scales necessary for parameterizing and testing regional- and global-scale terrestrial ecosystem and biosphere models (e.g., Potter et al. 2003, Anderson et al. 2008). In particular, satellite-based optical remote-sensing measurements of changes in surface reflectance have yielded global data sets on the dynamics of leaf-area index (LAI), vegetation greenness, and other measures of foliar vegetation on timescales ranging from days to decades at resolutions of kilometers or less (Nemani et al. 2003, Myneni et al. 2007). There are also numerous derived data sets regarding ecosystem properties and dynamics, such as land-cover classifications and land-use transitions (Masek et al. 2006, Hansen et al. 2008). However, optical remote sensing is not able to directly measure changes in woody biomass and other key metrics of vegetation structure, such as basal area and canopy height that are key variables for both diagnosing current ecosystem state, and predicting long-term changes in ecosystem composition and function. Instead, information on the composition and structure of forests (i.e., the relative abundance of trees of different species and their distribution across tree size classes and across horizontal

Manuscript received 11 February 2010; revised 13 August 2010; accepted 19 August 2010; final version received 10 September 2010. Corresponding Editor: A. D. McGuire.
[4] Corresponding author.
E-mail: paul_moorcraft@harvard.edu

space) has been obtained from laborious and expensive ground-based forest inventories of individual trees. As a result, the sample sizes and spatial extent of forest inventories are often small, and thus unable to provide comprehensive, region-wide information on the dynamics of vegetation structure and biomass in many areas of the globe. This is particularly true in the tropics, where comprehensive, regional-scale inventories are not generally available.

Light Detection and Ranging (Lidar) and Radio Detection and Ranging (Radar) measurements offer promising ways to obtain information on the dynamics of vegetation structure, at both the scale of individual trees (Popescu et al. 2003, Antonarakis et al. 2008) and the canopy (Drake et al. 2002, Saatchi et al. 2007, Sun et al. 2008). Lidar, due to its ability to measure the distance from the sensor to the surfaces in its path, has been used mainly to extract canopy heights. Radar pulses have the primarily to penetrate canopies of different densities depending on the wavelength of the pulse emitted, and thus have been used to estimate basal area, volume, and aboveground biomass (AGB) from radar backscatter measurements (Fransson et al. 2000, Quiñones and Hoekman 2004, Saatchi et al. 2007). The most recent Radar Interferometry techniques have extended the application of the Radar remote sensing in estimating forest heights (Cloude and Papathanassiou 1998, Sarabandi and Lin 2000, Askne et al. 2003, Treuhaft and Siqueira 2004).

In this study we analyze the ability of Radar and Lidar remote-sensing measurements to provide information on forest structure that can be assimilated into a terrestrial biosphere model, and, by doing so, constrain and improve its predictions of carbon fluxes and ecosystem dynamics. The model used in this analysis is the ED2 terrestrial biosphere model (Medvigy et al. 2009). Like its predecessor, ED2 uses a system of partial differential equations to approximate the behavior of a heterogeneous, spatially distributed ensemble of individual plants (Hurtt et al. 1998, Moorcroft et al. 2001, Moorcroft 2003). The equations and parameter values of ED2 thus incorporate the nonlinear impacts of fine-scale horizontal and vertical heterogeneity in ecosystem structure on both the plant-level carbon and water fluxes that underlie the canopy-scale exchange of CO_2 and H_2O with the atmosphere and the plant-level growth and mortality dynamics that underlie the long-term vegetation dynamics of the ecosystem (Moorcroft 2006, Medvigy et al. 2009). The model, therefore, can simulate the ecosystem dynamics and carbon fluxes at any spatial scale and can be readily integrated with spatially explicit data on the horizontal and vertical structure of the vegetation.

As discussed by Hurtt et al., (2004), several distinct approaches are used for initializing terrestrial ecosystem and biosphere models. By far the most widely used approach has been to initialize model simulations with an arbitrary initial condition (usually a near-bare-ground ecosystem), and then force the model with appropriate near-surface climate-forcing data until the model reaches its so-called "potential-vegtation" equilibrium for the locations(s) of interest. The problem with this potential-vegetation approach is that when evaluating a terrestrial ecosystem or biosphere model's predictions of vegetation dynamics, one is usually interested in assessing the model's so-called *process error*—errors arising from inaccuracies in the model formulation embodied in its current equations and parameter values. This is normally done by comparing its predictions of observable quantities such as an ecosystem's net rate of carbon exchange, or its rate of aboveground biomass accumulation within the ecosystem over a certain period of time (e.g., Braswell et al. 2005, Medvigy et al. 2009). However, there are two additional important sources of error that affect the model's predictions for an ecosystem. The first is the *forcing error*, error caused by inaccuracies in the climate data used to force the model simulation; the second is the *initialization error*, error in the model's ecosystem state at the beginning of the observation period. Minimizing these additional two sources of error is critical to improving resulting terrestrial ecosystem predictions.

For the forcing error, the best approach is to use, whenever possible, observed meteorology rather than meteorological reanalysis data, or output from an atmospheric model, to prescribe the necessary environmental forcings for the ecosystem or biosphere model. However, even in situations when observed meteorological forcing data are available, and thus there is minimal forcing error, it is unknown to what extent mismatches between the model predictions reflect process error, or simply initialization error arising from incorrect specification of the initial ecosystem state.

Minimizing initialization error is more challenging, since it requires information on the values of the model's state variables at the beginning of a simulation. In the case of terrestrial ecosystem and biosphere models, such as ED2, a critical state variable is the amount of aboveground biomass and the vertical and horizontal distributions of this quantity within the forest canopy. As shown by Medvigy et al. (2009), forest inventories can be used to specify the current structure and composition of the aboveground ecosystem and thereby reduce the initialization error. By doing so, it is possible to better identify and correct the model's process error, and thus improve its ability to predict the future fate of the ecosystem. Forest-inventory observations do not provide a complete description of vegetation state, since they do not provide information on the values of other vegetation-state variables, such as leaf biomass and amount of stored carbon. However, they crucially provide a near-complete specification for current state of the vegetation structure and composition within the area sampled, which governs its long-term decadal to century-scale dynamics of the ecosystem (Moorcroft et

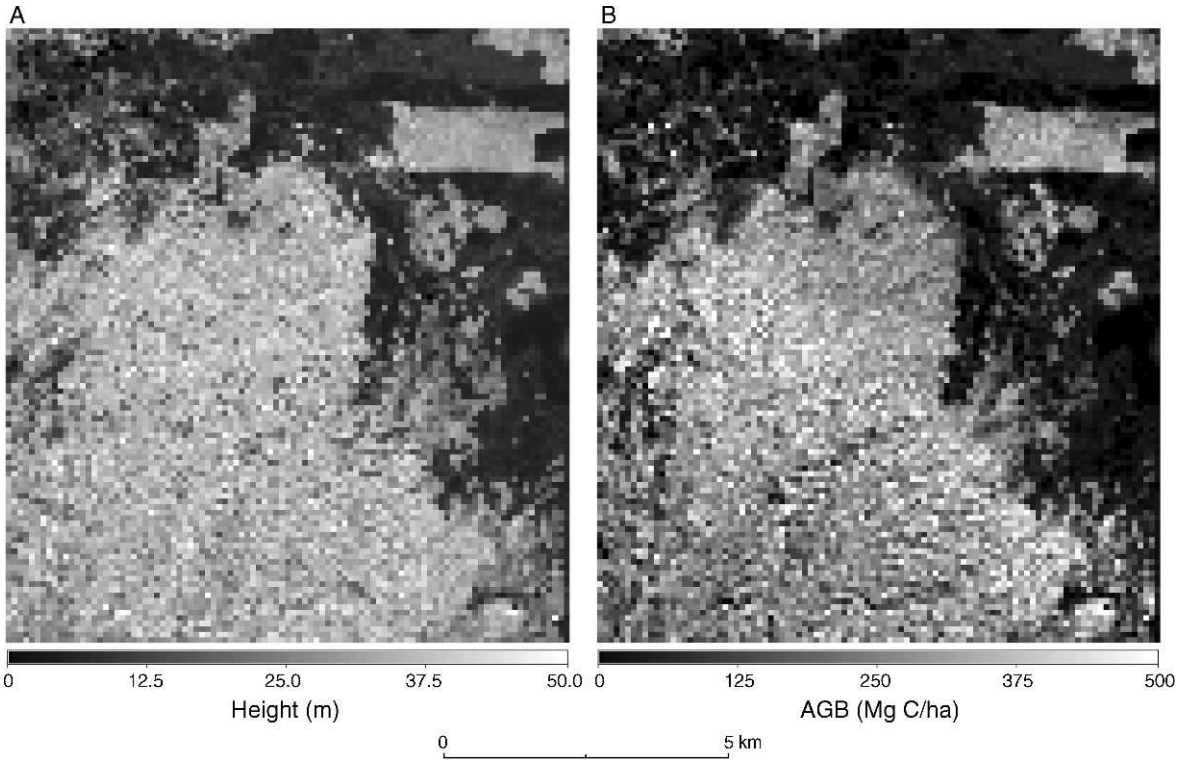

FIG. 1. Raster layer of (A) Lidar-derived canopy height and (B) Radar-derived aboveground biomass (AGB).

al. 2001). Moreover, as shown by Medvigy et al., (2009), the unknown values of other shorter-term carbon pools can be assessed by performing a short-term spin-up simulation (i.e., starting from a near-bare-ground initial condition) with observed environmental forcing.

As noted earlier, the problem with forest-inventory observations lies in their limited availability in many ecosystems, and lack of consistencies in the way in which the measurements are collected in different areas. These factors hinder the ability to conduct rigorous regional- and global-scale evaluations of terrestrial ecosystem and biosphere models.

In this analysis we explore how Lidar-derived canopy height and Radar-derived measurements of aboveground biomass can provide information on current ecosystem structure, and thus be used to constrain the predictions of terrestrial ecosystem and biosphere models, by reducing initialization error. Specifically, building on the earlier work of Hurtt et al. (2004), we compare ED2 biosphere-model simulations for the La Selva tropical forest ecosystem initialized with Radar and Lidar measurements against ED2 simulations initialized with potential vegetation, and against ED2 simulations initialized from forest-inventory measurements of vegetation structure and composition. Successful applications of these methods could pave the way for far more rigorous regional- and global-scale evaluations of terrestrial ecosystem and biosphere models.

STUDY AREA AND DATA

Study area

La Selva Biological Station in northeast Costa Rica (Fig. 1) is one of the most heavily studied tropical forests in the world (Clark 1988, McDade et al. 1994). This 1536-ha area is comprised of a mixture of lowland old-growth and secondary tropical wet forest (Holdridge et al. 1971, Guariguata et al. 1997, Clark and Clark 2000), abandoned pasture, current and abandoned plantations, and agroforestry plots (Menalled et al. 1998). Elevation ranges approximately 35–135 m above sea level, with a north–south gradient resulting in higher elevations and steeper slopes to the south where the reserve borders on the Braulio Carrillo National Park. The soils at La Selva are primarily a mixture of inceptisols in the north and residual ultisols to the south (Clark et al. 1998). The spatial heterogeneity in soil and topography affects stem size, density, stand dynamics, wood density, and aboveground biomass (Clark and Clark 2000, Baker et al. 2006, Chave et al. 2006, Saatchi et al. 2010). Because of the variety of land-cover types and the wealth of ancillary data (e.g., soil, topography, forest structure), La Selva is an excellent site for assessing the potential for remote-sensing measurements to measure spatial variation in tropical-forest biomass arising from both abiotic landscape heterogeneities and disturbance history.

Remote-sensing data

In March of 2004 the NASA/JPL (Jet Propulsion Laboratory) airborne SAR (synthetic-aperture radar) system (AIRSAR) acquired fully polarimetric images along with simultaneous interferometric TOPSAR data over the La Selva Biological Station. The polarized backscatter values derived from these measurements are HH, HV, and VV, where H and V represent the horizontal and vertical transmit and receive polarizations, respectively. The Radar data set used in this study was the fully polarimetric P-band (435 MHz, 20 MHz bandwidth) AIRSAR imagery acquired at 10-m spatial resolution over an 11-km-wide transect at incidence angles ranging from 20 to 60 degrees. All images were terrain corrected using the digital elevation data acquired by the TOPSAR interferometric modes and ground control points, and orthorectified into a Universal Transverse Mercator (UTM) projection using high-resolution optical remote-sensing data with a large number of ground control points that provided registration accuracy of ~15 m (1.5 pixels).

Saatchi et al. (2010) used the fully polarimetric P-band AIRSAR imagery in conjunction with ground-based forest inventory to estimate the spatial variation in aboveground biomass (AGB) across the La Selva site (Fig. 1). The radar backscatter image was upscaled to a 100-m spatial resolution to estimate the AGB at a scale where the spatial variability of forest structure due to small-scale disturbance is removed and the radar backscatter measurements are improved from the reduction of speckle noise (Saatchi et al. 2010). AGB values from radar backscatter were determined by using a statistical regression model between AGB and the backscatter at different polarizations. The model used was a multiple linear-regression model developed between the square root of the AGB and a linear combination of P-band backscatter measurements at three polarizations, as defined in Saatchi et al. (2010), as

$$\mathrm{AGB}^{0.5} = \alpha_0 + \alpha_1\gamma_{\mathrm{HH}} + \alpha_2\gamma_{\mathrm{HV}} + \alpha_3\gamma_{\mathrm{VV}} \qquad (1)$$

where the coefficients (α_0, α_1, α_2, and α_3) are determined statistically using allometrically derived biomass values from field trunk diameters, and the normalized P-band backscatter values (γ) at the different polarizations (HH, transmitted and received radiation was vertically polarized; HV, transmitted radiation was horizontally polarized and received radiation was horizontally polarized; VV, transmitted and received radiation was vertically polarized). The estimated P-band regression coefficients for 1.0-ha scale AGB at La Selva are: $\alpha_0 = 0.73$; $\alpha_1 = 42.13$; $\alpha_2 = 323.02$; $\alpha_3 = 71.51$ (Saatchi et al. 2010). The backscatter values were also normalized by the incidence angle of the transmitted polarizations (Saatchi et al. 2010).

In March 2005 the spatial pattern of canopy height at La Selva (Fig. 1) was determined using the laser vegetation-imaging sensor (LVIS), a medium-altitude, medium-to-large footprint imaging laser altimeter, designed and developed at NASA's Goddard Space Flight Center. LVIS digitizes the entire return signal, thus providing a waveform relating to the vertical distribution of intercepted canopy and ground surfaces within each LVIS footprint (Blair et al. 1999, Dubayah and Drake 2000, Dubayah et al. 2000). The digital elevation model (DEM) was determined from the LVIS ground return, and was initially gridded at a 20-m resolution. This was measured as the elevation above sea level and had an absolute accuracy of ±3.37 m (Saatchi et al. 2010). The original 10-m radar backscatter image was co-registered with this 20-m DEM, to a registration error of <10 m. In this analysis we used RH100, the difference between the height of the first Lidar-return and the ground-return signal that provides a measure of the maximum height of the forest canopy within each Lidar footprint. These values were upscaled to 100-m pixels by averaging the RH100 values derived from the LVIS shots.

Forest-inventory measurements

Ground-based measurements of forest structure were available from the Transect (Saatchi et al. 2010) and Bosques (Chazdon et al. 2005) forest-inventory plots for a mixture of old-growth and secondary forests. For the Transect plots, all stem diameters of trees greater than 10 cm in seven plots corresponding to a total area of 5.5 ha were measured, and the species of each stem was identified. For the Bosques plots, all stem diameters of trees greater than 5 cm in two plots with plot sizes of 1 ha were measured and the species of each stem was identified. All the tree-level data used for model initializations were weighted by their respective plot sample areas. The species found within these plots were classified into the ED2 terrestrail biosphere model plant functional types (see next section) based on their wood density determined using the data sets of Chave et al. (2006) and the FAO (Brown 1997). The ED2 plant functional-type classifications described in Moorcroft et al. (2001) are defined by the relationship between the plant's wood density (ρ) and its leaf longevity (l), where $\rho = 0.5 + 0.2(l - 1)$. Here, early successional plants are denoted as having a leaf life span of one year with a resulting wood density of 0.5 g/cm^2, mid-successional plants as having a leaf life span of two years with a resulting wood density of 0.7 g/cm^2, and late-successional plants as having a leaf life span of three years with a resulting wood density of 0.9 g/cm^2. It should be noted that work is currently being done to better define these density thresholds for Central American trees. Of the over 6000 trees measured in the field, 83.5% of the individuals were categorized as being early successional trees, 16.1% as mid-successional trees, and 0.4% as late-successional trees.

Model and Methods

ED2 terrestrial biosphere model

The ED2 terrestrial biosphere model (Fig. 2) simulates vegetation dynamics using integrated submodels of plant growth and mortality, phenology, disturbance, biodiversity, hydrology, and soil biogeochemistry, and a system of size- and age-structured partial differential equations to approximate the behavior of an individual-based spatially distributed collection of plants within each climatological grid cell (Moorcroft et al. 2001, Medvigy et al. 2009). These equations track the changing abundance of trees of different sizes and plant functional types arising from tree growth, mortality, recruitment, and the impact of disturbances. The partial differential equations are defined as

$$\underbrace{\frac{\partial}{\partial t}n^{(i)}(z,a,t)}_{\text{change in plant density}} = \underbrace{-\frac{\partial}{\partial z}[g^{(i)}(z,\bar{\mathbf{r}},t)\,n^{(i)}(z,a,t)]}_{\text{plant growth}} - \underbrace{\frac{\partial}{\partial a}n^{(i)}(z,a,t)}_{\text{aging of plant community}} - \underbrace{\mu^{(i)}(z,\bar{\mathbf{r}},t)\,n^{(i)}(z,a,t)}_{\text{mortality}} \quad (2)$$

$$\underbrace{\frac{\partial}{\partial t}p(a,t)}_{\text{change in age structure}} = \underbrace{-\frac{\partial}{\partial a}p(a,t)}_{\text{aging}} - \underbrace{\lambda(a,t)p(a,t)}_{\text{disturbance}} \quad (3)$$

where

$$\frac{\partial}{\partial z} = \left\{\frac{\partial}{\partial z_s}, \frac{\partial}{\partial z_a}\right\} \qquad \int_0^\infty p(a,t)\,da = 1$$

and where Eq. 2 relates the change in expected plant density (n) with the growth rate, mortality rate, and aging of a plant community of functional type i, where z is the size of individuals, a is the time since last disturbance, $\bar{\mathbf{r}}$ is a vector describing the resource environment (light, water, nitrogen) experienced by an individual of a certain size, and t is time. The functions $g^{(i)}(z, \bar{\mathbf{r}}, t)$ and $\mu^{(i)}(z, \bar{\mathbf{r}}, t)$ represent the growth and mortality factors at any time t. The growth can be further described as an array of structural (z_s) and active tissue (z_a) growth compartments. Eq. 3 describes the changes in the distribution of landscape ages since the last disturbance event, where $\lambda(a, t)$ is the rate of disturbance. For both Eqs. 2 and 3 a boundary condition is the recruitment of new seedlings corresponding to a flux of individuals into the system at (z_0, a) under the assumption of random dispersal of seeds between gaps within a grid cell, and Eq. 2 has a second boundary condition, describing the state of the ecosystem following a disturbance event related to the survivorship of individuals following the disturbance event of the plant of type i and size z. Finally, Eq. 3 has a boundary condition describing the fraction of newly disturbed areas within a grid cell (see Moorcroft et al. [2001] for further details).

The size and age structure approximation is completed by initial conditions corresponding to the initial size distribution for Eq. 2 and to the initial age distribution for Eq. 3 of the plant types:

$$\underbrace{n^{(i)}(z,a,0) = n_0^{(i)}(z,a)}_{\text{initial plant community}} \qquad \underbrace{p(a,t_0) = p_0(a)}_{\text{initial age disturbance}}. \quad (4)$$

With this system of equations ED2 is able to represent the dynamics of spatially heterogeneous forest communities that arise due to natural disturbances, such as fire, and anthropogenic disturbances, such as forest harvesting or land clearing (e.g., Hurtt et al. 2004, Albani et al. 2006, Medvigy et al. 2009). Plants within each climatological grid cell experience the same meteorological forcing, specified either from a meteorological forcing data set or from the boundary conditions of an atmospheric model (Fig. 2A). Each grid cell is subdivided into a series of dynamic horizontal tiles representing areas of forest that share a similar vegetation canopy structure and disturbance history. Long-term vegetation dynamics are produced by integrating short-term carbon dynamics (Fig. 2B) of individual plants which, in turn, drive the dynamics of canopy mortality, growth, and recruitment in Eq. 2 (Fig. 2C). Each plant functional type i also differs in terms of its leaf physiology and wood density that result in different rates of growth and mortality and sensitivity to environmental conditions. Following Moorcroft et al. (2001), four tropical-plant functional types were represented; C_4 grasses, early, mid-, and late-successional trees. Since a palm plant functional type was not available, the 12% of stems that were palms were assigned to one of the three tree functional types based on their wood density. With the exception of *Welfia regia*, this resulted in all palms being categorized as early successional, with *W. regia* being classified as mid-successional.

The temperature, precipitation, humidity, wind, and pressure meteorological forcing variables for the model simulations were specified from measurements at the La Selva meteorological station spanning the period 1992–2005. Since earlier analyses have indicated that the radiation measurements available at La Selva appear to be unreliable due to inaccuracies in the instrument at high temperatures and humidity (D. A. Clark, *personal communication*), the shortwave and longwave radiation forcing was specified from the National Centers for Environmental Predictions/National Center for Atmospheric Research (NCEP/NCAR) Reanalysis data, which is a continuation from the similar Climate Data Assimilation System (CDAS) (Kalnay et al. 1996). The spatial grid cell of the climate data is larger than the ED2 modeling grid cell, indicating that all forest types within the model grid cells are exposed to the same climate forcing.

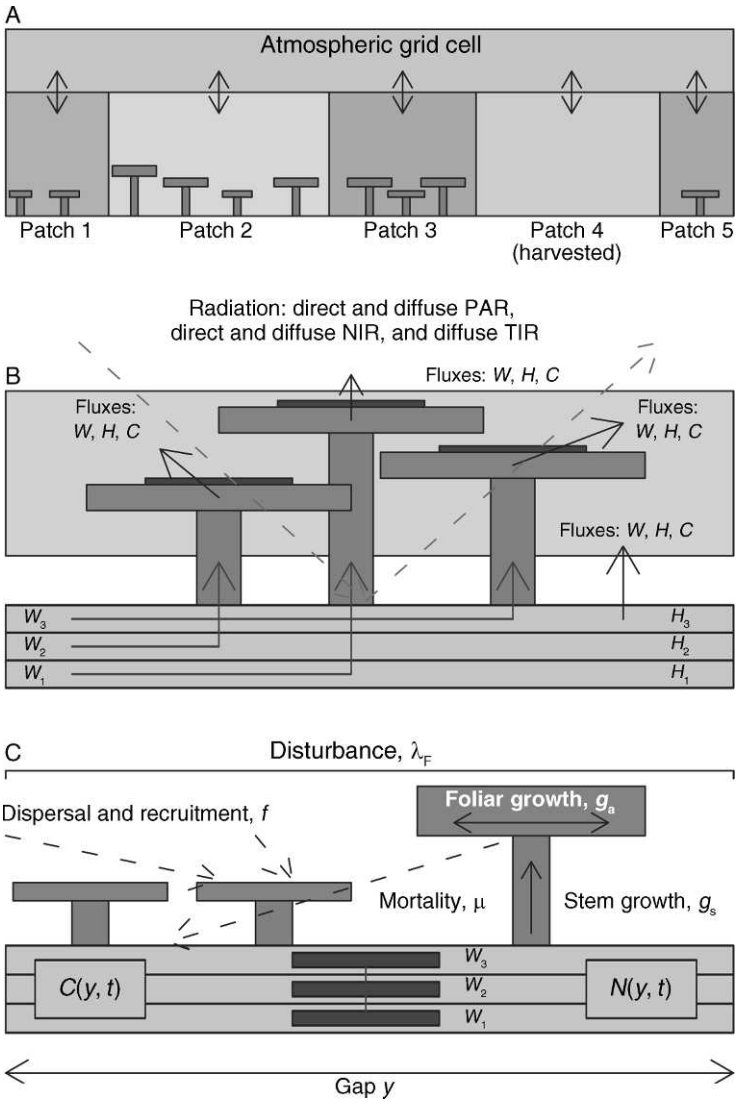

FIG. 2. Schematic figure representing the ED2 terrestrial-biosphere model structure and process. (A) Each grid is subdivided into tiles with the relative area of each tile determined by the proportion of canopy-gap-sized areas having a similar forest structure due to a similar disturbance history. (B) Within each tile, the multilayer short-term canopy fluxes of water (W), internal energy (H), and carbon (C) are calculated. Abbreviations: PAR, photosynthetically active radiation; NIR, near infrared; and TIR, thermal infrared. (C) An illustration of the long-term vegetation dynamics in heterogeneous plant communities resulting from the short-term fluxes. The growth is represented in terms of stem and active tissue growth (g_s, g_a), the mortality as a rate μ, recruitment at rate f within and between gaps, and disturbance at rate λ_F (from Medvigy et al. 2009). Other abbreviations: N, nitrogen; y, gap; and t, time.

Analysis

As noted in the *Introduction*, we conducted ED2 simulations using four different sources of initialization data. The first was a traditional potential-vegetation (PV)-initialized simulation, in which the model was initialized with output from a long-term simulation that began in 1500 with nearly bare ground and continued to the present, yielding a forest structure that is in dynamic equilibrium with the climate-forcing data. For all runs the climate driver was prescribed by sequentially cycling over the 1992–2005 data set. The second type of initialization data set was calculated from the ground-based observations of forest structure following the procedure of Medvigy et al. (2009). Because the canopy-gap-scale distribution of times since last disturbance within the inventory observations $p(a, t_0)$ is not known, horizontal heterogeneity in canopy composition was represented explicitly by grouping the inventoried plots into a series of distinct subgrid-scale tiles based on their similarity in vertical structure and composition. The compositional profile within each tile was then defined, assigning all trees to their corresponding plant functional type based on their wood density values as defined

in *Study area and data: Forest inventory measurements*, above.

The third kind of initialization utilized Radar-derived spatial distribution of aboveground biomass AGB(X, Y) (Fig. 1B) to constrain the distribution of aboveground biomass within the simulation domain at the beginning of the simulation. The equivalent aboveground biomass (AGB) distribution in the ED2 model is

$$\mathrm{AGB}(a, t_0)p(a, t_0) \quad (5)$$

where $p(a, t_0)$ is landscape-scale age *distribution* at the beginning of the simulation (t_0), and $AGB(a, t_0)$ is the *aboveground biomass* related to the canopy-gap age at the beginning of the simulation. Using the approach of Hurtt et al. (2004), the ED2 model distribution ($p(a, t_0)$) in Expression 5 can be adjusted to match the Radar-derived *biomass distribution*, for equivalent biomass values, thereby providing an empirical constraint on the state of the aboveground ecosystem at the beginning of the simulation.

Unlike the forest-inventory data, Radar-derived biomass (AGB(X, Y)) does not uniquely specify the state of the ecosystem (Eq. 4), because it does not provide the breakdown of biomass across size classes and plant functional types.

An estimate for this breakdown comes from the output from the potential-vegtation (PV) simulation: i.e.,

$$n^{(i)}(z, a, t_0) \propto n_{PV}^{(i)}(z, a, t_{\max}) \quad (6)$$

where $n^{(i)}(z, a, t_0)$ is the distribution of stems at the beginning of the model simulation and $n_{\mathrm{PV}}^{(i)}(z, a, t_{\max})$ is the distribution of stems at the end of the PV simulation. Adjusting the PV simulation biomass distribution with the Radar-derived values, results in an altered distribution of aboveground biomass across size classes and plant functional types.

The fourth initialization was produced in a similar manner, but this time using the spatial distribution of canopy height values $H(X, Y)$ obtained from the Lidar measurements to constrain the equivalent distribution in ED2 model:

$$H(a, t_0)p(a, t_0). \quad (7)$$

Here, $H(a, t_0)$ is the relationship between *canopy height* and canopy-gap age, with the breakdown of across-size classes and plant functional types again specified using Eq. 6. Again, Lidar-derived *canopy height fractional areas* are used to adjust fractional areas from the equivalent height value class in the ED2 model. Fig. 3 illustrates the model initialization procedure by highlighting the steps involved in matching the Radar AGB and Lidar height data with the potential-vegtation simulation output.

Data fusion

The Radar and Lidar initializations described in the previous section constrain forest structure, but provide no information on forest composition. In the approaches described in the *Analysis* section, the composition information is provided by the output of the PV simulation. Since errors in composition also have a significant influence on the model's predictions, we explored the effects of using additional information—in this case the forest-inventory data—to correct errors in forest composition. A flow chart summarizing this composition-correction method is shown in Fig. 4A. As before, the Radar biomass (AGB(X, Y)) and Lidar heights ($H(X, Y)$) were used to adjust the PV forest structure distributions (Eqs. 5 and 7), however now, the breakdown of size classes and plant functional types from the PV simulation described in Eq. 6 is used in these re-initializations, altering the potential-vegtation plant types ($n^{(i)}(z, a, t_0)$), to match the forest-inventory plant types. This was done by specifying the proportion of plant functional types in each diameter class from the forest inventory and applying this to the Radar and Lidar initializations.

In a subsequent approach we exercised another form of data fusion in which the full forest inventory plots are used, as they provide detailed information on the actual distribution and composition. This fusion links the spatially heterogeneous Lidar canopy-height and Radar biomass measurements to the fine-scale distributions of height and biomass across size classes. The fusion technique is described in the flow chart in Fig. 4B. From the plant density and diameter-at-breast-height (dbh) information measured in the field, ED2 allometry was used in order to determine the height and biomass associated with each individual tree. ED2 relates the height of each individual tree to its dbh, where the slope and intercept is specific to the plant functional type. Aboveground biomass is determined for a plant functional type of a certain height, from a combination of stem, sapwood, leaf, seeds, and storage components of biomass. These resulting structure metrics aggregated at the patch level are adjusted with the proportions of each AGB and height value determined from Radar and Lidar data before re-initializing.

Results

The prior distributions (circles) and adjusted distributions (crosses) of aboveground biomass (AGB) and canopy heights (H) are shown in Fig. 5A and B, respectively. The distribution of AGB in the potential-vegetation (PV) simulation (circles) is negatively skewed, reflecting the model's assumption of a constant, spatially uniform rate of disturbance (see *Model and methods: ED2 biomass model*, above), which yields a negative exponential distribution of canopy-gap ages. In contrast, the distributions of AGB and H determined from the Radar and Lidar measurements (triangles) at 100-m (0.1-ha) grid cells are generally more normally distributed, suggesting a landscape-scale equilibrium state for forest structure and biomass at that scale. The results also suggest that the PV model cannot simulate the

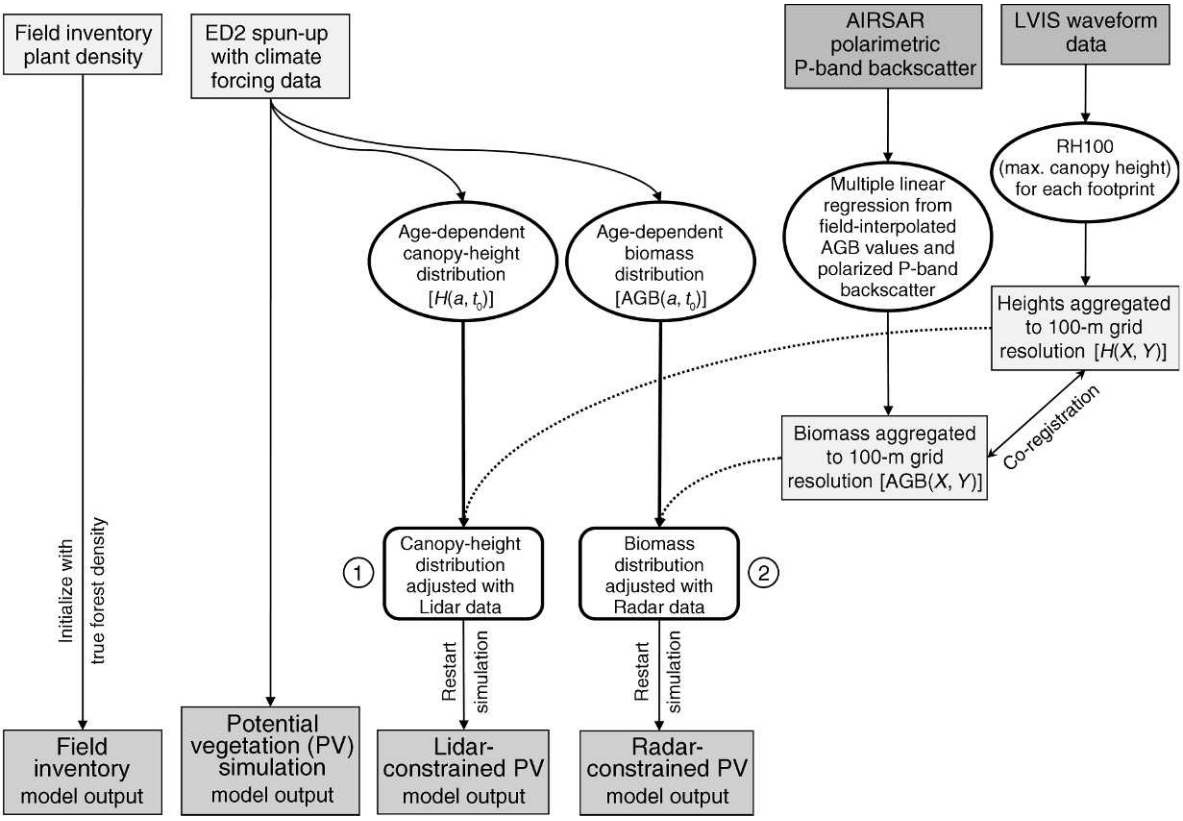

FIG. 3. Flow chart illustrating the ED2 biosphere model simulations performed in this study, and the integration of Radar and Lidar data into the model. The circled numbers 1 and 2 are reference points for simulations described elsewhere in the paper. Abbreviation key: AIRSAR, airborne synthetic-aperture radar; LVIS, laser vegetation-imaging sensor; AGB, aboveground biomass; RH100, maximum canopy height; a, time since last disturbance; t_0, time at beginning of simulation.

forest structure accurately at that prescribed scale. The Lidar-derived distribution of canopy heights is slightly negatively skewed, likely reflecting the underlying averaged RH100 criterion for determining canopy height from Lidar waveform data at the 100-cm grid cell.

Forest structure

The forest structure of the four initializations are shown in Fig. 6, with visualizations of the stand structure, and the accompanying distribution of forest basal area and aboveground biomass across tree-diameter classes. In the forest-inventory initialization (Fig. 6A), most of the basal area and biomass is located in the 0–100 cm diameter range, with 28% and 10% of the basal area distributed in the >60-cm- and >100- cm-diameter class ranges, respectively. In contrast, in the original potential-vegetation (PV) simulation (Fig. 6B), basal area and AGB are spread across a larger range of size classes (range: 0–240 cm) with 54% and 34% of the forest basal area in the >60 cm and >100 cm ranges, respectively. There are also differences in composition between forest-inventory and PV simulation. In the forest-inventory approach, 88% of the basal area is early successional trees, with the majority of the remainder belonging to the mid-successional plant functional type. In contrast, in the PV simulation only 31% of the trees are early successional, with 69% late successional.

Both the Radar-derived (Fig. 6C) and Lidar-derived (Fig. 6D) initializations yield basal area and AGB diameter-class distributions that are significantly closer to the observed forest structure than did the PV simulation. Both forms of remote-sensing initializations have basal area and AGB diameter distributions that are close to the size distributions of the forest-inventory initialization. In the case of the Radar initialization (Fig. 6C), the resulting forest structure has 22% and 11% of its basal area located in the >60-cm- and >100-cm-diameter class ranges. In the Lidar-derived initialization (Fig. 6D), 25% and 17% of the basal area is located in the >60-cm- and >100-cm-diameter class ranges. Note however that while both the Radar-derived and Lidar-derived initializations significantly constrain the above-ground ecosystem structure, neither correct for the inaccurate distribution of trees across successional types in the PV simulation (as indicated by the color of the trees and the color of the bars of the basal area and AGB distributions in Fig. 6).

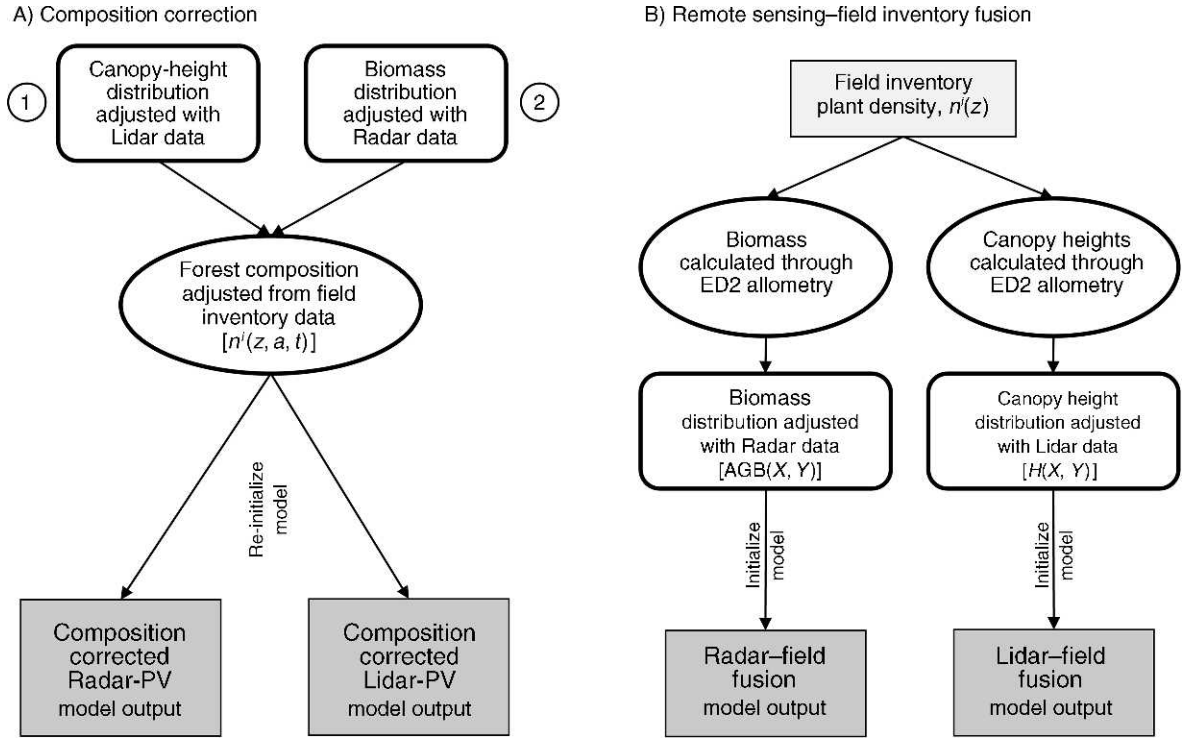

FIG. 4. Flow chart illustrating the ED2 simulations performed in order to correct for (A) composition, and for (B) composition and structure. The circled numbers 1 and 2 are reference points from the flow chart in Fig. 3.

Dynamics of forest structure

Trends in ED2 model simulations of the aboveground biomass, vegetation height, basal area, and leaf-area index (LAI) from 2004–2008 after being initialized with the potential vegetation, radar, lidar and forest-inventory data sets in 2004 are shown in Fig. 7A.

The PV initialization produces AGB values that are considerably higher than those obtained from the model with forest-inventory observations (~24.3 kg/m^2 vs. ~12.5 kg/m^2 respectively) (Fig. 7A, first row). In contrast, the Radar-initialized simulation has AGB values closer to those obtained from forest-inventory initialization, with an average AGB of 15.5 kg/m^2 over the observation period, and with an average difference of 21% compared to 90% for the potential-vegtation simulation. The Lidar-initialization yields a more modest improvement to the AGB dynamics with an average difference of 54%, and average AGB values of 19.5 kg/m^2.

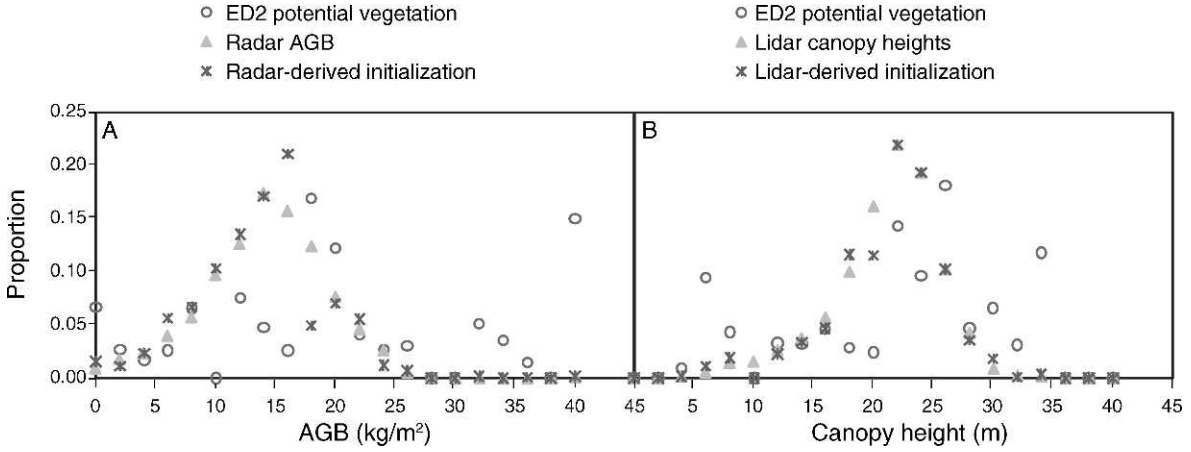

FIG. 5. Distribution of (A) aboveground-biomass (AGB) values and (B) canopy-height values. Initializing the ED2 terrestrial biosphere model with known forest-attribute distributions required adjusting the equilibrium-run distributions to the Radar- and Lidar-derived biomass and canopy-height distributions.

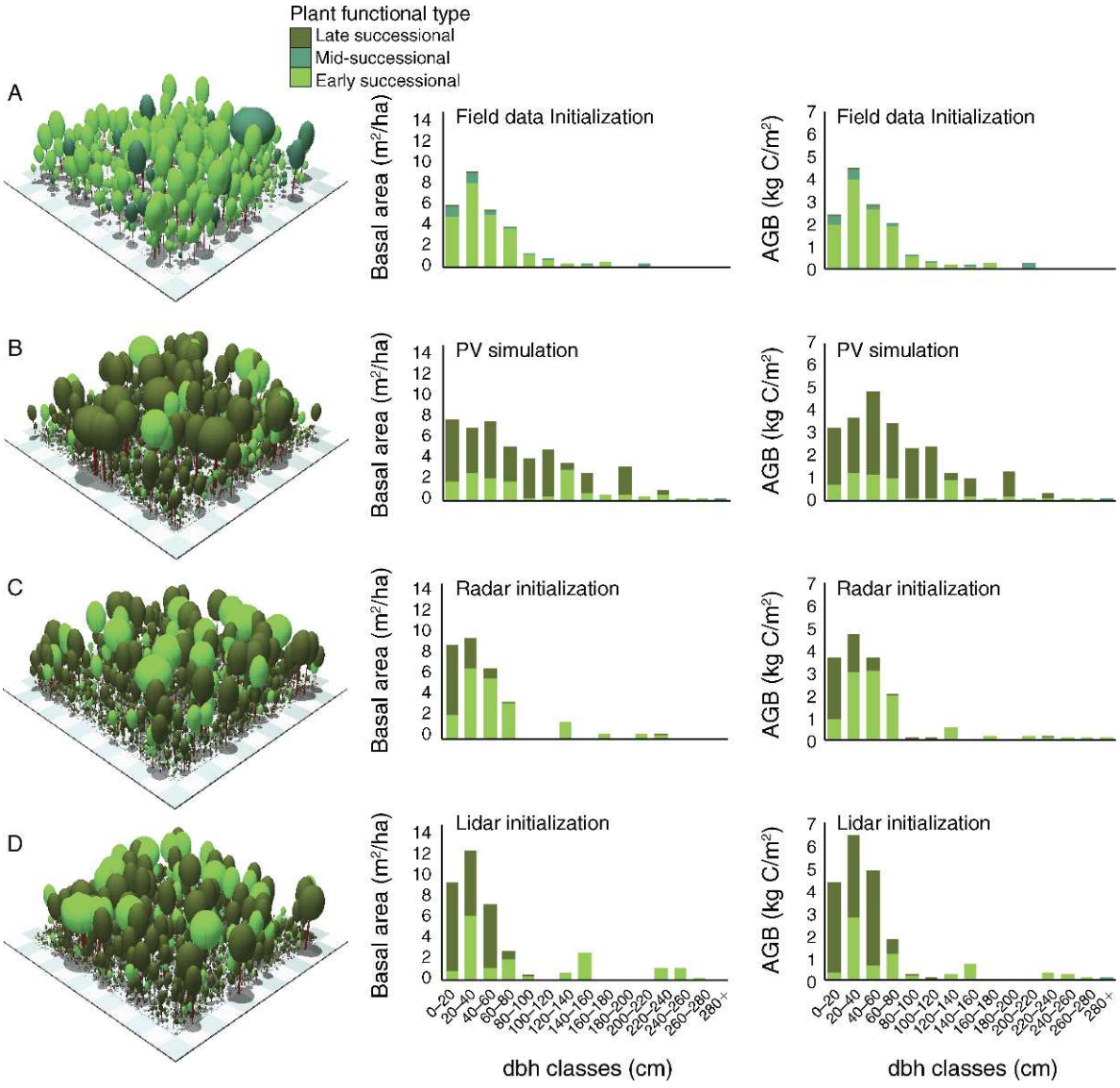

FIG. 6. For the beginning of each of the four simulations, dbh classes for basal area (BA) (middle column) and for aboveground biomass (AGB; right column) are presented. Ray-tracing visualizations (left column) of the cohorts (tree crowns) are also presented with the color coding corresponding to the succession stage. The Radar- and Lidar-initialized simulations are compared to the potential-vegetation (PV) simulation begun in 1500, and to the simulation initialized from the forestry-inventory data.

In comparision to the dynamics of AGB, the canopy-height dynamics obtained from the PV initialization estimations are close to those output from the forest-inventory initialization (compare red and blue lines in Fig. 7A, second row). Canopy-height values in the forest-inventory simulation are, on average 22.5 m, compared to around 23.2 m in the PV simulation, a difference of only 3.2% over the simulation period. In the Lidar-initialized simulation (green in Fig. 7A, second row), this discrepancy is reduced slightly, to only 1.9%. In contrast, the Radar initialization yields canopy-height values that are further from the forest-inventory initialized simulation than the PV simulation, with values that on average are 1.8 m (9%) lower than the forest-inventory initialization. A primary reason for the poor performance of the AGB initialization for the average height simulations is the large variance in AGB and height relationships.

The dynamics of basal area (BA) are similar to those of AGB values derived from Radar and Lidar initializations, with average differences of 14% and 36%, respectively, compared to the forest-inventory initialization. The difference between the potential-vegtation simulation and the forest inventory is again the largest, with differences of up to 70% (Fig. 7A, third row). The LAI is the only metric in Fig. 7A where the Radar and

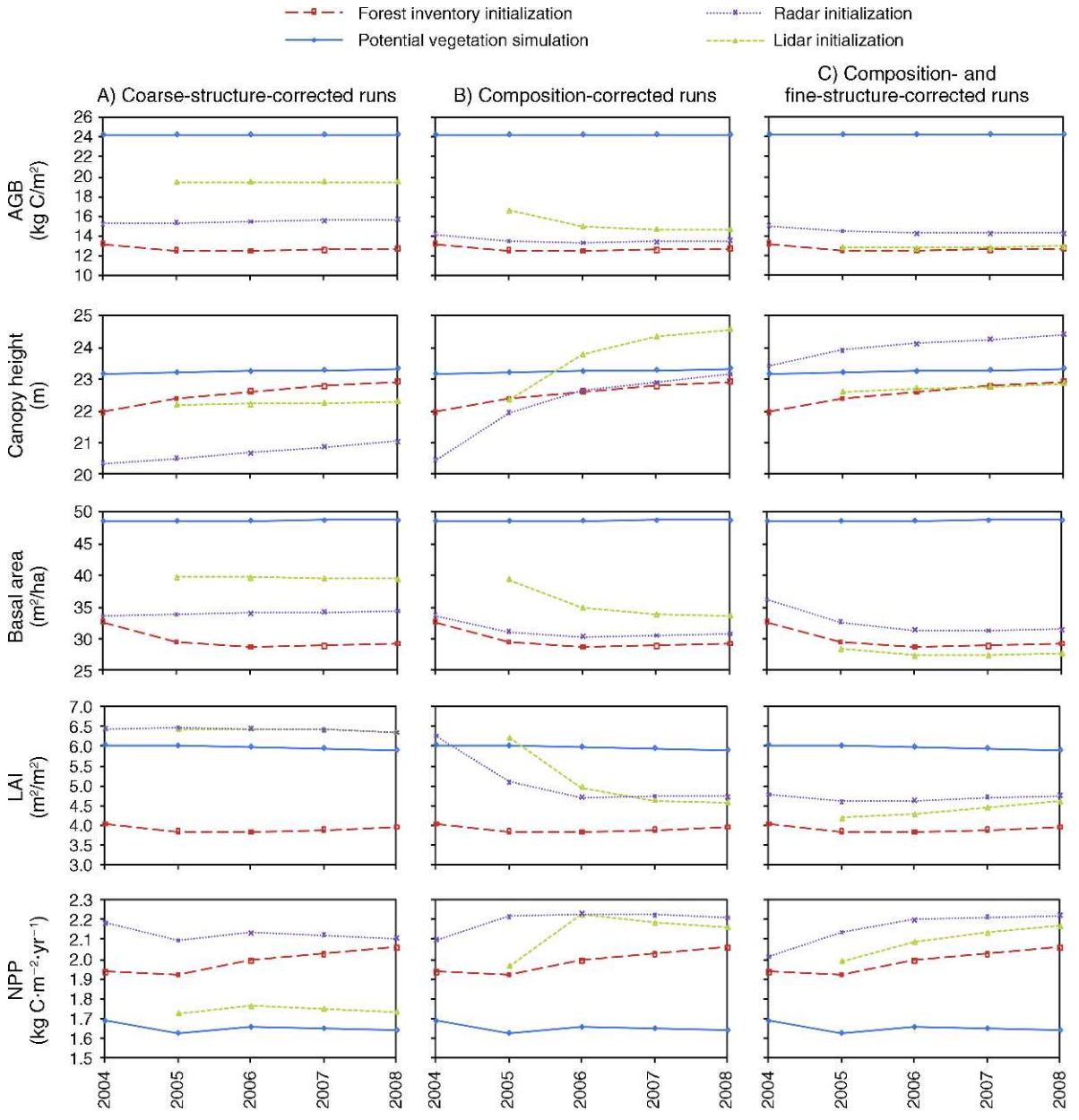

FIG. 7. Direct forest-structure variables plotted from 2004–2008 for aboveground biomass (AGB), vegetation height, basal area (BA), leaf-area index (LAI), and a carbon-flux variable: net carbon primary production (NPP). The Radar- and Lidar-initialized simulations are compared to the potential vegetation (PV), and to the initialization from field data. The ecosystem-dynamics results are from the three data-assimilation methods; the columns present three runs: (A) original Radar- and Lidar-initialized simulations; (B) composition-corrected Radar- and Lidar-initialized simulations; and (C) composition-corrected and fine-scale structure-corrected Radar- and Lidar-initialized simulations. Details on the correction methodologies are given in *Models and methods: Data fusion.*

Lidar initializations do not substantially constrain the PV simulation, but rather there is a small rise in LAI of about 0.45 m^2/m^2 from the PV dynamics.

Forest structure from data-fusion methods

In the first fusion initialization approaches described in *Model and methods: Data fusion*, above, Radar and Lidar information were combined with the forest-composition information from the forest inventory in order to better constrain the model's predictions. The new Radar and Lidar composition-corrected initializations now have the same structure, but with composition that matches that found in the forest inventory (Fig. 6A). The actual composition of the forest is 85–90% early successional, with most of the rest belonging to the mid-successional functional type. This forest-composi-

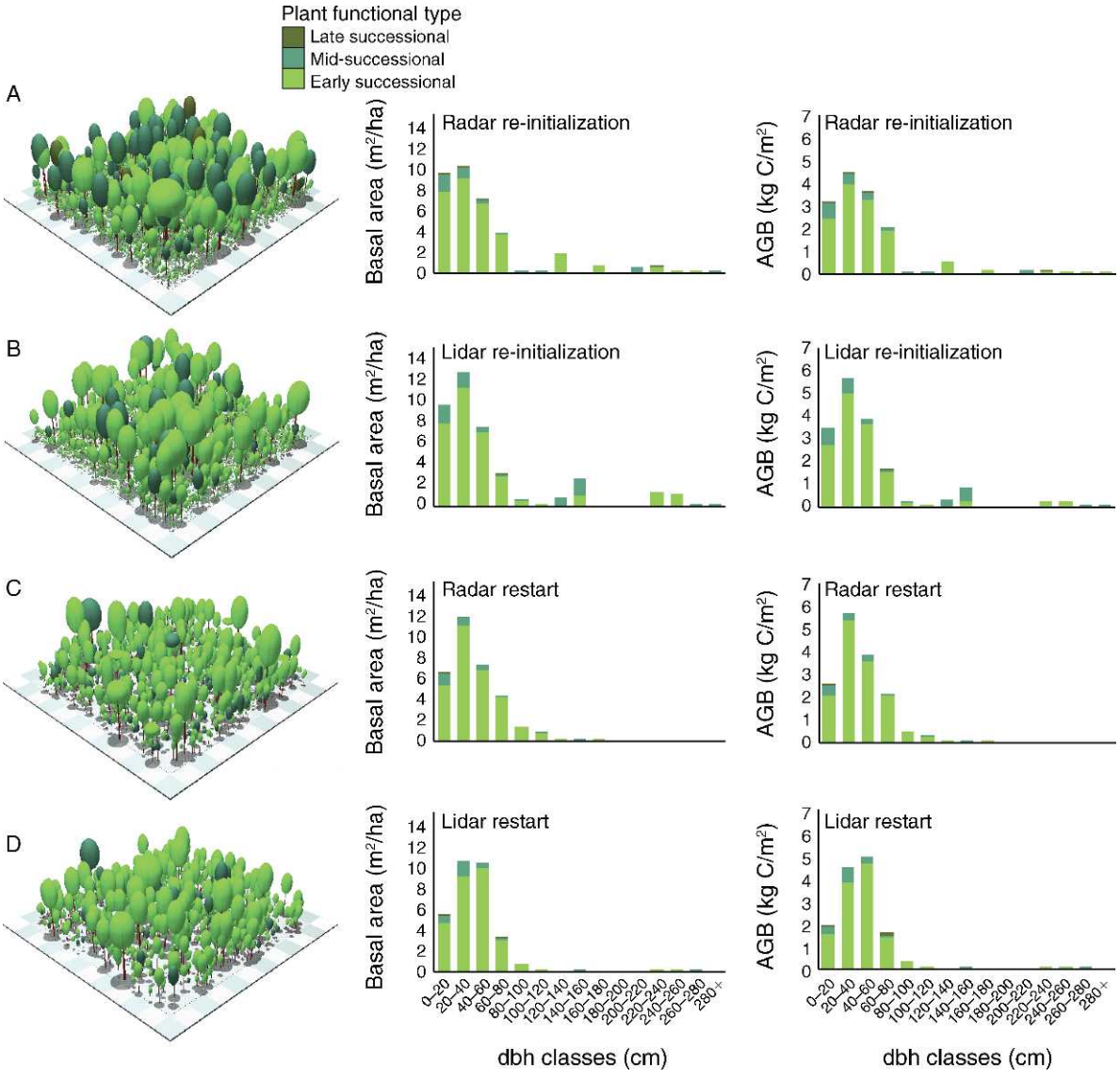

FIG. 8. Ray tracing stand visualizations with their corresponding aboveground-biomass distribution with dbh size classes. The (A) Radar and (B) Lidar composition corrections result from the re-initialization-model output from the simulations described in the flow chart (Fig. 4A). The subsequent (C) Radar and (D) Lidar composition-and-structure corrections result from the restart-model output from the simulations described in the flow chart (Fig. 4B).

tion correction is illustrated in Fig. 8A and B. In the second fusion approach described in the *Data fusion* section (above), Radar and Lidar information was fused with the forest inventory in order to tie in height and biomass across space, with the fine-scale distribution of height and biomass across size classes. The fused Radar and Lidar–forest-inventory initializations (Fig. 8C, D), now have both forest structure and composition very close to the forest-inventory initializations (Fig. 6A). The stand is ~85–90% early successional for both remote-sensing fusion initializations, with Radar and Lidar AGB on average 1.7 and 0.3 kg C/m^2 different, respectively, from the original forest-inventory-derived AGB values.

Dynamics of forest structure from data-fusion methods

Fig. 7B, top row, shows the AGB dynamics obtained from Radar and Lidar initializations that are corrected for forest composition. The patterns through the period indicate a decrease in AGB by ~14% for the Radar and 28% for the Lidar composition-corrected runs. Fig. 7C, top row, shows the AGB dynamics obtained when the Radar and Lidar initializations are corrected for both forest composition and fine-scale canopy structure using the remote-sensing–forest-inventory fusion method. This yields AGB values for the Radar and Lidar fused initializations to be on average 13% and 2% higher, respectively, than the forest-inventory plots.

Application of the composition correction to the Radar- and Lidar-initialized simulations significantly changes the dynamics of canopy height (see Fig. 7B, second row). While the canopy-height values obtained from the PV-initialized simulation remain close to the forest-inventory initialized simulation, in both the composition-corrected Radar and composition-corrected Lidar simulations, average canopy height increases by ~10–13%, a dynamic that is more consistent with the canopy-height dynamics seen in the forest-inventory-initialized simulation (Fig. 7B, second row). This contrasts with the original Radar- and Lidar-initialized simulations in which canopy height remained stable or increased slightly over the four-year simulation period (Fig. 7A, second row). In addition, the composition-corrected Radar simulation is closer to the forest-inventory simulation than the composition-corrected Lidar simulation, with an average difference of 1.5% compared to the forest-inventory-initialized simulation (Fig. 7B, second row). This pattern is reversed, however, in the composition- plus structure-corrected Radar and Lidar simulations (Fig. 7C, second row). In these simulations the canopy-height dynamics in the composition- plus structure-corrected Lidar simulation differs <1% from the field-inventory-initialized simulation, while the composition-and-structure-corrected Radar simulation is ~7% greater than field-inventory initialization.

Application of the composition correction to the Radar- and Lidar-initialized simulations also significantly improves the model's basal-area dynamics (Fig. 7B, third row). Both the composition-corrected Radar and composition-corrected Lidar simulations yield basal areas that are closer to the forest-inventory-initialized simulation by around 8% and 11%, respectively. As with AGB, the trajectories of basal area (BA) over the simulation period are also closer to the forest-inventory-initialized simulations. While in the original Radar- and Lidar-initialized simulations BA remained near constant over the four-year simulation (Fig. 7A, third row), BAvalues now decline by ~10–15% over the course of the simulation, a dynamic that is more consistent with the dynamics seen in the forest-inventory-initialized simulation (Fig. 7B, third row). The composition and structure-corrected Radar and Lidar simulations are closer still with BA values (Fig. 7C, third row) that are, respectively, 10% greater and 4% lower than the forest-inventory simulation.

The dynamics of leaf-area index (LAI) in the composition-corrected Lidar and Radar simulations are shown in Fig. 7B, fourth row. In contrast to the earlier Radar and Lidar initialized simulations in which LAI dynamics were not improved over the PV (potential-vegetation) simulation, application of the composition correction in both Radar and Lidar initializations improved the dynamics of LAI. In both simulations, the initial LAI is still significantly overestimated (LAI of 6.5 vs. 4), but then declines to around 5, while the forest-inventory-initialized simulation LAI is between 4.1 and 3.9 over the course of the simulation. Applying the composition and structure correction in Radar and Lidar–field fusion further corrects the LAI. The initial Radar and Lidar LAI values differs by 0.7 and 0.3, respectively, from the forest-inventory simulation, but as the simulation continues, these LAI values increase to around 4.8 and 4.6, respectively (Fig. 7C, fourth row).

Forest growth and mortality

The dynamics of growth and mortality for all simulations are shown in Fig. 9. As Fig. 9A, top row, shows, the rate of basal-area (BA) growth in the forest-inventory-initialized simulation (red line) increases markedly over the simulation period from 0.4 $m^2 \cdot ha^{-1} \cdot yr^{-1}$ to 2.3 $m^2 \cdot ha^{-1} \cdot yr^{-1}$ while in the potential-vegtation (PV) simulation BA growth remains at a near constant value of 1.6 $m^2 \cdot ha^{-1} \cdot yr^{-1}$ throughout the simulation period (blue line). Both the Radar-initialized (purple dotted line) and Lidar-initialized (green dashed line) simulations exhibit patterns of growth that are largely unchanged from that of the PV simulation, with near-constant growth rates of 2.1 and 1.6 $m^2 \cdot ha^{-1} \cdot yr^{-1}$, respectively, throughout the simulation. Application of the composition correction (Fig. 9B, top row) results in a slight increase in BA growth to the Radar-initialized and Lidar-initialized simulations; but, in both, the rate of growth remains too high. However, application of the composition and structure correction to both the Radar-initialized and Lidar-initialized simulations (Fig. 9C, top row) yields dynamics that closely follow the pattern of increasing BA growth observed in the forest-inventory-initialized simulation (Fig. 9C, top row).

With regard to mortality dynamics, the forest-inventory-initialized simulation (red line) has a high rate of BA mortality of ~3 $m^2 \cdot ha^{-1} \cdot yr^{-1}$ during the first two years of the simulation, which then declines to ~1.6 $m^2 \cdot ha^{-1} \cdot yr^{-1}$ during the second two years of the simulation. In contrast, the PV simulation (blue line) has a low, and relatively constant rate of basal area loss of ~1.2 $m^2 \cdot ha^{-1} \cdot yr^{-1}$. Initialization of the model with either the Radar and Lidar (purple line and green lines) does not significantly change the pattern of BA mortality from the pattern seen in the PV simulation. In both simulations mortality is slightly higher than the PV results due to the shifting of forest structure to the smaller diameter-size classes, and the resulting increase in the proportion of early successional trees in the model simulation, which have higher rates of mortality than the mid- and late-successional plant functional types. As seen in Fig. 9B, bottom row, application of the composition correction results in a marked increase of BA mortality in the Radar-initialized simulation during the second year of the simulation (purple dotted line), and a marked increase in the mortality in the Lidar-initialized simulation during the third year of the simulation (green dashed line). Applying the composition and the structure correction to the Radar- and Lidar-initialized simulations results in BA mortality

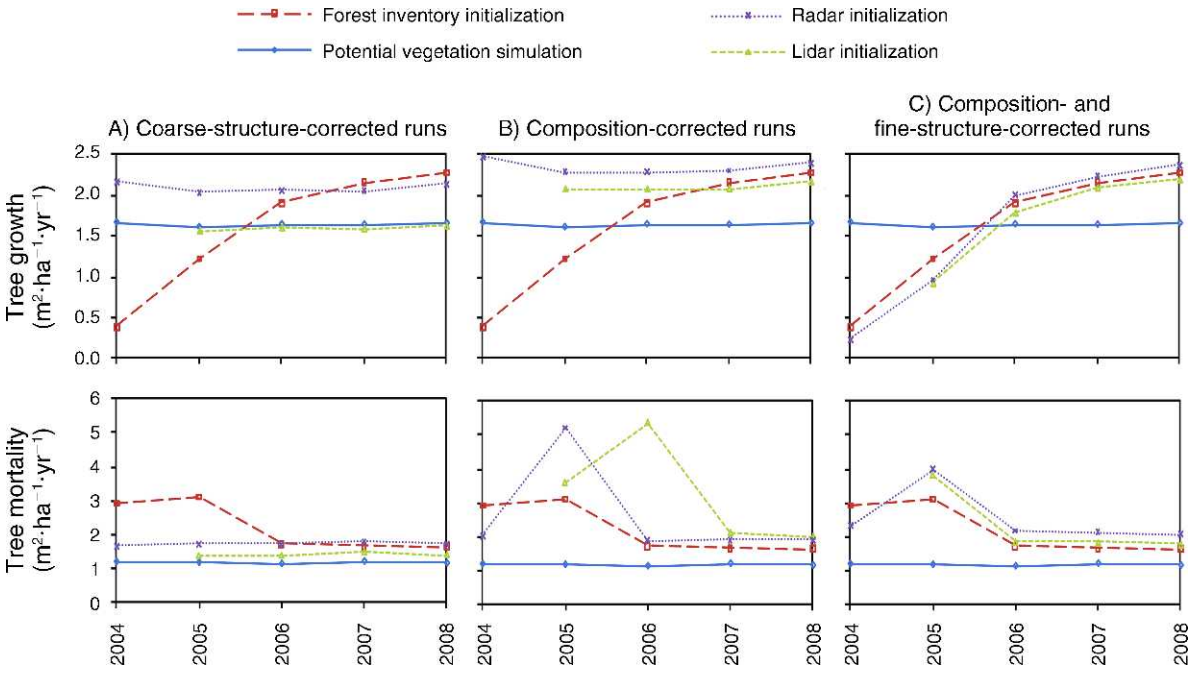

FIG. 9. Basal-area tree growth (BA gained; top row of panels) and mortality (BA lost; bottom row) for the simulated period. (A) Growth and mortality from the four original plots. (B) Growth and mortality values for Radar and Lidar initializations corrected for forest composition in order to match the true composition in the field. (C) Growth and mortality values where the Radar and Lidar forest information is fused with the field data so that they match the structure and composition of the field. The calculated increment is the value obtained from field measurements of all trees in a 1-ha plot measured in 2004 and 2007.

dynamics that are very similar to the forest-inventory-initialization simulation (Fig. 9C, bottom row).

Carbon fluxes

Fig. 7, bottom row, shows the dynamics of net primary production (NPP) calculated as gross primary productivity minus autotrophic respiration, for the potential-vegtation, forest-inventory and Radar- and Lidar-initialized simulations. As can be seen in the figure, the NPP resulting from the forest-inventory-initialization simulation (red line) is around 1.9–2 kg $C \cdot m^{-2} \cdot yr^{-1}$, while the NPP of the PV simulation (blue line) is ~17% lower at around 1.65–1.7 kg $C \cdot m^{-2} \cdot yr^{-1}$. Both the Radar- and Lidar-initialized simulations (purple and green lines respectively) have NPP values that are closer to the forest-inventory-initialized simulation than the PV simulation with values around 2.1–2.2 and 1.73–1.77 kg $C \cdot m^{-2} \cdot yr^{-1}$, respectively, which are, on average, 7% and 13% different, respectively, than the forest-inventory-initialized NPP values.

Applying the composition correction to the Radar-initialized simulation produces only a slight change in the NPP dynamics (compare the purple lines in Fig. 7A and B, bottom row), increasing the NPP by ~3%. Applying the composition correction to the Lidar-initialized simulation produces a 22% increase in NPP (compare the green lines in Fig. 7A and B, bottom row. Correcting the Radar-initialized simulation for both composition and structure results in little change in the Radar-initialized simulation. (compare the red lines in Fig. 7A and C, bottom row); however, correcting the Lidar- initialized simulation for both composition and structure reduces its NPP (compare the green lines in Fig. 7B and C, bottom row) yielding NPP values closer to the forest-inventory initialization.

DISCUSSION

This study has shown how estimates of aboveground biomass (AGB) and canopy height (H) obtained from Radar and Lidar active remote-sensing measurements can be used to constrain the predictions of terrestrial ecosystem and biosphere models. Radar backscatter intensity has been widely used to estimate AGB (e.g., Quiñones and Heokman 2004, Saatchi et al. 2007, 2010), and Lidar signals have been widely used to determine canopy heights (e.g., Dubayah and Drake 2000, Popescu et al. 2003, Sun et al. 2008), but the use of such products to constrain terrestrial ecosystem and biosphere model predictions of ecosystem dynamics and ecosystem function is still in its infancy. As shown here, the use of Radar and Lidar information to initialize terrestrial ecosystem and biosphere models is important because those measurements provide information about the actual vegetation structure present at a given location rather than assuming, as is current practice, that vegetation is simply in equilibrium with its current climate and disturbance forcing. In doing so, active remote-sensing estimates of forest structure supply important constraints

on terrestrial ecosystem and biosphere model predictions of current and future ecosystem structure and function by reducing initialization error. As described in the *Introduction* (above), the scientific value of reducing the model-initialization error is that it constrains the value of key unknown model state variables at the beginning of a simulation, and by doing so, can improve model predictions and facilitate the identification and correction of process-level errors in the underlying model formulation. Specifically, the analyses conducted here for the La Selva Tropical Forest (Costa Rica) showed how Radar and Lidar data indicate a lower number of larger trees than was estimated by a potential-vegtation (PV) simulation, and that incorporating this information into the model initialization yields a model whose vegetation structure more closely matched the observed size-class distribution of the forest. They also significantly constrained the dynamics of AGB, basal area (BA), and net primary production (NPP) through the five-year simulated period. The Radar and Lidar initializations did not, however, decrease the dominance of late-successional functional types in the PV simulation, since they only provide structural rather than compositional information. As our subsequent simulations showed, when Radar and Lidar information on forest structure was combined with forest-inventory information on forest composition, this resulted in further constraining of the AGB, BA, and even leaf-area index (LAI) as a result of better-constrained mortality patterns. To quantify the remaining error in the model initialization, we performed a more complete large-scale to fine-scale fusion of Radar and Lidar with the forest inventory to best represent the forest structure and composition. This final approach yielded a forest structure, composition, and dynamics that were closest to the forest-inventory-initialized simulation. These results suggest that, with current technologies, more accurate estimations of changes in carbon stocks and fluxes for any site requires fusion of hectare-scale information on forest structure with information on fine-scale forest structure. Further details and explanations of these general findings are given below.

Initializing with the Radar and Lidar reduces the abundance of tree sizes in larger size classes, more closely reflecting the forest-inventory tree size distributions, and this improves the dynamics of forest structure. This is because the distributions of AGB and canopy heights were different for the PV simulation and the Radar- and Lidar-derived variables (Fig. 5). Understanding the genesis of the differences in these distributions provides insight into process-level errors in the model formulation. The distributions of AGB and canopy heights in the potential-vegtation (PV) simulation were both negatively skewed (Fig. 5). The reason for this is that the PV simulation assumes, for simplicity, a constant, spatially uniform, rate of canopy-gap disturbance, resulting in an exponential distribution of times since disturbance (see *Model and Methods: ED2 biosphere model*, above). Since both AGB and height increase approximately monotonically with time since disturbance, this results in both quantities having distributions that are also skewed towards larger size classes. In contrast, the distributions of AGB and canopy heights derived from both Radar and Lidar measurements are more normally distributed. Several factors account for this difference. First, evidence suggests that the rate of disturbance increases as a function of canopy age (Richards 1952, Whitmore 1982, Johnson et al. 1995). The consequence of this effect is to truncate the long tail in the height and diameter distributions on the landscape that would otherwise have arisen as it does in the PV simulation. In future analyses, the recent availability of disturbance-dynamics data sets, such as that from the Landsat archive (e.g., Ferraz et al. 2009, Li et al. 2009, Huang et al. 2010), offers a promising way to more accurately specify the history of disturbance within a given ecosystem. A second factor is that the distributions of Radar-derived AGB and Lidar-derived heights reflect spatial variation in these quantities at the hectare scale (~100 m) while the distribution in PV simulation reflects the spatial variation at the scale of canopy tree gaps (~10 m). The Radar and Lidar distributions thus average over the canopy gap-scale distribution present in the PV simulation.

As Fig. 6 also shows, associated with the errors in forest structure in the PV simulation are errors in composition. Specifically, as would be expected given the historical disturbance regime in the PV simulation, it has an excess of late-successional trees and insufficient abundance of early successional trees, compared to the forest inventory (compare Fig. 6A and B). The improved representation of forest structure following initialization with the Lidar and Radar data partially reduces the canopy-composition error by increasing the abundance of early successional trees (see Fig. 6C, D); however, errors in composition still remain.

To quantify the effects of the remaining error in forest composition, we evaluated a fusion approach that used information on composition from the forest inventory to produce composition-corrected Lidar and Radar initializations (see Fig. 8A, B), with a dominance of early successional trees (~87% of the basal area) similar to the forest inventory. Both composition-corrected Radar- and Lidar-initialized simulations resulted in more realistic canopy dynamics compared to the forest-inventory dynamics. These more realistic canopy dynamics can be explained by composition-corrected mortality patterns that more closely fit the forest-inventory mortality dynamics. Here, Radar and Lidar composition-corrected initializations give rise to marked increases in mortality in the second simulation year (~6 $m^2 \cdot m^{-2} \cdot yr^{-1}$; Fig. 9B), similar to the forest inventory. This is a result of increasing the proportion of early successional trees, which have higher rates of mortality than later functional types due to their lower wood density (Moorcroft et al. 2001, Muller-Landau 2004, King et al. 2006).

In the second fusion approach, we combined Radar and Lidar information on large-scale forest structure with the fine-scale information on forest structure and composition from the forest-inventory measurements. This approach, not surprisingly, yields a forest structure, composition, and dynamics that were closest to the forest-inventory-initialized simulations, with all variables considered being <20% different from the forest inventory, (see Figs. 7C and 9C). As these figures show, the dynamics arising from this second fusion method are similar to, but different from, those produced by the forest-inventory-initialized simulation, thereby illustrating how the remote-sensing data bring additional information regarding the large-scale spatial structure of the forest that is not captured in the 7.5 ha of forest-inventory plots. These results imply that techniques that combine information about forest structure collected at different spatial scales offer the most promise for providing an accurate quantification of aboveground ecosystem state. As shown here, this can be achieved either by fusion of Lidar and Radar data collected at a relatively coarse (1-ha) scale with ground-based forest-inventory data. An interesting topic for further study is whether similar results can be obtained by fusion of hectare-scale Lidar and Radar data with active remote-sensing measurements of sub-hectare variation in canopy structure.

An important question for understanding the terrestrial carbon cycle is whether active remote-sensing estimates of forest structure can sufficiently constrain the carbon dynamics of the ecosystem. In this study, we focused on net primary productivity, since NPP is the key diagnostic of the carbon dynamics of the aboveground ecosystem, and unlike net ecosystem productivity, NPP is not affected by magnitude of the belowground soil carbon pools. For the original four simulations, the Radar and Lidar initializations appear to constrain the PV simulation by raising the annual NPP towards that of the forest-inventory initialization. However, this constraining of Radar- and Lidar-initialization NPP values from the PV simulation actually arose from a fortuitous compensating error. The potential-vegtation (PV) simulation had a significantly higher LAI and total aboveground biomass compared to the forest-inventory–initialized simulation (see Fig. 7A, first and fourth rows), but its resulting NPP is significantly lower than the NPP of the forest-inventory-initialized simulation (see Fig. 7A, bottom row). This apparent paradox can be explained by considering how the LAI and AGB are distributed across size classes. As noted earlier, the PV simulation results in a forest that contains an excess of late-successional trees. This larger proportion of late-successional trees reduces NPP because of their lower photosynthetic capacity compared to earlier successional trees (see Moorcroft et al. 2001), and this exceeds the increased photosynthesis that arises from the increased LAI.

As seen in Fig. 6, initialization with either the Radar AGB or Lidar height data partially reduces the excess proportion of late-successional trees in the canopy, and by doing so, increases the NPP in the Radar- and Lidar-initialized simulation towards that seen on the forest-inventory-initialized simulation. However, as discussed earlier, both the Lidar and Radar initializations also result in an excess of smaller sized trees (see Fig. 6). In the ED2 terrestrial biosphpere model, canopy-scale NPP is higher when trees are smaller, primarily because of decreased respiration costs per unit AGB in smaller trees compared to larger trees. Note that this mechanism is in accordance with observations (e.g., Mäkelä and Valentine 2001); however, there is also evidence that other mechanisms, such as increased nutrient availability and the absence of reproduction can also contribute to the higher productivity of younger, smaller-statured stands (Ryan et al. 1997). Thus the excess of abundance of smaller-tree size classes has the effect of further increasing the canopy-scale average NPP. In other words, the error in the size distribution compensates for error in the NPP arising from the over-abundance of remaining late-successional trees in the Radar- and Lidar-initialized simulations. A follow-on consequence of this is that the mismatch between the composition-corrected Radar and the forest-inventory-initialized simulation is larger than the mismatch between the Radar-initialized simulation and the forest-inventory-initialized simulation, because it removed the partially compensating reduction in NPP values that arose from having more late-successional tress than is actually observed. This same phenomenon also occurs when comparing the composition-corrected Lidar simulation vs. the Lidar-initialized simulation.

This study has demonstrated the ability of large-footprint airborne Lidar and Radar in obtaining forest-structure data at an appropriate scale in order to constrain predictions on forest ecosystem structure and function. At least for the tropical forest considered here, the Radar-initialization data consisting of a P-band-derived estimate of the spatial distribution of aboveground biomass (AGB) provides a better constraint on the model's dynamics that the Lidar-derived initialization via canopy that utilizes the spatial distribution of canopy heights. This is particularly true especially concerning the distribution of biomass and basal areas across tree-diameter classes. The Radar initialization correctly reduces the amount of basal area to the first 60-cm size classes and lower overall basal area and biomass compared to the Lidar-based initialization. Moreover, as seen in Fig. 7B, the composition-corrected Radar simulation is more similar to the dynamics of the forest-inventory-initialized simulation than the composition-corrected Lidar simulation even for canopy height. This is likely due to the fact that P-band Radar estimates of forest biomass are based on a signal that interacts not only with the dominant and tallest trees, but also with the lower canopy and understory. In

contrast, the Lidar RH100 maximum-canopy-height estimate is unaffected by the presence or absence of the smaller-sized trees that are below the dominant crown. Interestingly, however, when combined with forest-inventory data on fine-scale structure, the Lidar-derived initialization is better than the corresponding Radar-derived initialization (see Fig. 7C).

The results from this study suggest that Radar- and Lidar-derived estimates of forest-canopy structure from future satellite missions such as the DESDynI (Deformation, Ecosystem Structure and Dynamics of Ice) mission (information *available online*)[5] will provide a unique, spatially consistent, source of information on aboveground ecosystem structure that can be used to constrain terrestrial ecosystem and biosphere models at global scales. An important future research direction will be to evaluate methods that exploit the complementary information on forest structure that Lidar and Radar provide. In particular, since Lidar is a near-nadir technique, it is sensitive to height and vertical profile of the forest while Radar measures reflected pulses at off-nadir and is sensitive to wood volume and density. Another interesting avenue for future work is investigating fusion methods that combine active remote-sensing wall-to-wall estimates of forest structure collected at hectare scales with active remote-sensing samples of sub-hectare canopy variation. As shown here, and by Thomas et al. (2008), for terrestrial biosphere models such as ED2 that track fine-scale spatial heterogeneity in ecosystem structure, incorporating information on large-scale and fine-scale ecosystem heterogeneity is critical for accurate prediction of the ecosystem's subsequent dynamics. Finally, as the results here suggest, from the perspective of constraining the dynamics of terrestrial biosphere models with remote-sensing measurements, an important next step is evaluating fusion methods that combine full-signal, active remote sensing of forest structure with hyperspectral measurements of forest composition in order to simultaneously constrain both the forest's structure and its composition (e.g., Treuhaft et al. 2004, Asner et al. 2008, Asner and Martin 2009).

Acknowledgments

The authors acknowledge the National Aeronautics and Space Administration (NASA) NNH05ZDA001N-RSSCC grant entitled "Remote Sensing Science for Carbon and Climate". We thank the NASA AIRSAR crew for the acquisition of the radar images and the JPL airborne SAR group for processing and calibration of the data. We thank the Goddard Space Flight Center for the availability of the LVIS data. We also thank R. Dubayah and B. Blair for advice and comments on the analysis. Our special thanks go to the La Selva Biological Station of the Organization for Tropical Studies.

Literature Cited

Albani, M., D. Medvigy, G. C. Hurtt, and P. R. Moorcroft. 2006. The contributions of land-use change, CO_2 fertilization, and climate variability to the Eastern US carbon sink. Global Change Biology 12:2370–2390.

Anderson, M. C., J. M. Norman, W. P. Kustas, R. Houborg, P. J. Starks, and N. Agam. 2008. A thermal-based remote sensing technique for routine mapping of land-surface carbon, water and energy fluxes from field to regional scales. Remote Sensing of Environment 112:4227–4241.

Antonarakis, A. S., K. Richards, J. Brasington, E. Muller, and M. Bithell. 2008. The use of Airborne Lidar to retrieve vegetative fluid resistance terms for rigid stems. Journal of Geographical Research-Biogeosciences 113, G02S07.

Askne, J., M. Santoro, G. Smith, and J. E. S. Fransson. 2003. Multitemporal repeat-pass SAR interferometry of boreal forests. IEEE Transactions on Geoscience & Remote Sensing 41:1540–1550.

Asner, G. P., D. E. Knapp, T. Kennedy-Bowdoin, M. O. Jones, R. E. Martin, J. Boardman, and R. F. Hughes. 2008. Invasive species detection in Hawaiian rainforests using airborne imaging spectroscopy and LiDAR. Remote Sensing of Environment 112:1942–1955.

Asner, G. P., and R. E. Martin. 2009. Airborne spectranomics: mapping canopy chemical and taxonomic diversity in tropical forests. Frontiers in Ecology and the Environment 7:269–276.

Baker, T. R., et al. 2004. Variation in wood density determines spatial patterns in Amazonian forest biomass. Global Change Biology 10:545–562.

Blair, J. B., D. L. Rabine, and M. A. Hofton. 1999. The laser vegetation imaging sensor (LVIS): a medium-altitude, digitations-only, laser altimeter for mapping vegetation and topography. ISPRS Journal of Photogrammetry and Remote Sensing 54:115–122.

Braswell, B. H., W. J. Sacks, E. Linder, and D. S. Schimel. 2005. Estimating diurnal to annual ecosystem parameters by synthesis of a carbon flux model with eddy covariance net ecosystem exchange observations. Global Change Biology 11:335–355.

Brown, S. 1997. Estimating biomass and biomass change in tropical forests: a primer. FAO Forestry Paper 134. Food and Agriculture Organization of the United Nations, Rome, Italy.

Chave, J., H. C. Muller-Landau, T. R. Baker, T. A. Easdale, H. ter Steege, and C. O. Webb. 2006. Regional and phylogenetic variation of wood density across 2456 neotropical tree species. Ecological Applications 16:2356–2367.

Chazdon, R. L., A. Redondo Brenes, and B. Vilchez Alvarado. 2005. Effects of climate and stand age on annual tree dynamics in tropical second-growth rain forests. Ecology 86:1808–1815.

Clark, D. A. 1988. Research on tropical plant biology at the La Selva Biological Station, Costa Rica. Evolutionary Trends in Plants 2:75–78.

Clark, D. B., and D. A. Clark. 2000. Landscape-scale variation in forest structure and biomass in a tropical rain forest. Forest Ecology and Management 137(1–3):185–198.

Clark, D. B., D. A. Clark, and J. M. Read. 1998. Edaphic variation and the mesoscale distribution of tree species in a neotropical rain forest. Journal of Ecology 86:101–112.

Cloude, S. R., and K. P. Papathanassiou. 1998. Polarimetric SAR interferometry. IEEE Transactions on Geoscience and Remote Sensing 36:1551–1565.

Drake, J. B., R. O. Dubayah, D. B. Clark, R. G. Knox, J. B. Blair, M. A. Hofton, R. L. Chazdon, J. F. Weishampel, and S. Prince. 2002. Estimation of tropical forest structural characteristics using large-footprint Lidar. Remote Sensing of Environment 79:305–319.

Dubayah, R. O., and J. B. Drake. 2000. Lidar remote sensing for forestry. Journal of Forestry 98(6):44–46.

Dubayah, R. O., R. G. Knox, M. A. Hofton, J. B. Blair, and J. B. Drake. 2000. Land surface characterization using lidar remote sensing. Pages 25–38 *in* M. J. Hill and R. J. Aspinall,

[5] ⟨http://nasascience.nasa.gov/missions/desdyni⟩

editors. Spatial information for land use management. International Publishers Direct, Singapore.

Ferraz, S. F. de B., C. A. Vettorazzi, and D. M. Theobald. 2009. Using indicators of deforestation and land-use dynamics to support conservation strategies: a case study of central Rondonia, Brazil. Forest Ecology and Management 257:1586–1595.

Fransson, J. E. S., F. Walter, and L. M. H. Ulander. 2000. Estimation of forest parameters using CARABAS-II VHF SAR data. IEEE Transactions on Geoscience and Remote Sensing 38:720–727.

Guariguata, M. R., R. L. Chazdon, J. S. Denslow, J. M. Dupuy, and L. Anderson. 1997. Structure and floristics of secondary and old-growth forest stands in lowland Costa Rica. Plant Ecology 132(1):107–120.

Hansen, M. C., Y. E. Shimabukuro, P. Potapov, and K. Pittman. 2008. Comparing annual MODIS and PRODES forest cover change data for advancing monitoring of Brazilian forest cover. Remote Sensing of Environment 112:3784–3793.

Holdridge, L. R., W. C. Grenke, W. H. Hatheway, T. Liang, and J. A. Tosi, Jr. 1971. Forest environments in tropical life zones: a pilot study. Pergamon Press, Oxford, UK.

Huang, C. Q., S. N. Coward, J. G. Masek, N. Thomas, Z. Zhu, and J. E. Vogelmann. 2010. An automated approach for reconstructing recent forest disturbance history using dense Landsat time series stacks. Remote Sensing of Environment 114:183–198.

Hurtt, G. C., R. Dubayah, J. Drake, P. M. Moorcroft, S. W. Pacala, J. B. Blair, and M. G. Fearon. 2004. Beyond potential vegetation: combining Lidar data and a height-structured model for carbon studies. Ecological Applications 14:873–883.

Hurtt, G. C., P. R. Moorcroft, S. W. Pacala, and S. A. Levin. 1998. Terrestrial models and global change: challenges for the future. Global Change Biology 4:581–590.

Johnson, E. A., K. Miyanishi, and J. M. H. Weir. 1995. Old-growth, disturbance, and ecosystem management. Canadian Journal of Botany 73:918–926.

Kalnay, E., et al. 1996. The NCEP-NCAR 40-year reanalysis project. Bulletin of the American Meteorological Society 77:437–471.

King, D. A., S. J. Davies, S. Tan, and N. S. M. Noor. 2006. The role of wood density and stem support costs in the growth and mortality of tropical trees. Journal of Ecology 94:670–680.

Li, M. S., C. Q. Huang, Z. L. Zhu, H. Shi, H. Lu, and S. K. Peng. 2009. Assessing rates of forest change and fragmentation in Alabama, USA, using the vegetation change tracker model. Forest Ecology and Management 257:1480–1488.

Mäkelä, A., and H. T. Valentine. 2001. The ratio of NPP to GPP: evidence of change over the course of stand development. Tree Physiology 24:1015–1030.

Masek, J. G., E. F. Vermote, N. E. Saleous, R. Wolfe, F. G. Hall, K. F. Huemmrich, F. Gao, J. Kutler, and T. K. Lim. 2006. A Landsat surface reflectance dataset for North America, 1990–2000. IEEE Geoscience and Remote Sensing Letters 3(1):68–72.

McDade, L. A., K. S. Bawa, H. A. Hespenheide, and G. S. Hartshorn. 1994. La Selva: ecology and natural history of a Neotropical rain forest. University of Chicago Press, Chicago, Illinois, USA.

Medvigy, D., S. C. Wofsy, J. W. Munger, D. Y. Hollinger, and P. R. Moorcroft. 2009. Mechanistic scaling of ecosystem function and dynamics in space and time: Ecosystem Demography model version 2. Journal of Geophysical Research 114:G01002.

Menalled, F. D., M. J. Kelty, and J. J. Ewel. 1998. Canopy development in tropical tree plantations: a comparison of species mixtures and monocultures. Forest Ecology and Management 104(1–3):249–263.

Moorcroft, P. R. 2003. Recent advances in ecosystem–atmosphere interactions: an ecological perspective. Proceedings of the Royal Society B 270(1521):1215–1227.

Moorcroft, P. R. 2006. How close are we to a predictive science of the biosphere? Trends in Ecology and Evolution 21(7):400–407.

Moorcroft, P. R., G. C. Hurtt, and S. W. Pacala. 2001. A method for scaling vegetation dynamics: the ecosystem demography model (ED). Ecological Monographs 71:557–585.

Muller-Landau, H. C. 2004. Interspecific and inter-site variation in wood specific gravity of tropical trees. Biotropica 36:20–32.

Myneni, R. B., et al. 2007. Large seasonal swings in leaf area of Amazon rainforests. Proceedings of the National Academy of Sciences USA 104:4820–4823.

Nemani, R. R., C. D. Keeling, H. Hashimoto, W. M. Jolly, S. C. Piper, C. J. Tucker, R. B. Myneni, and S. W. Running. 2003. Climate-driven increases in global terrestrial net primary production from 1982 to 1999. Science 300:1560–1563.

Popescu, S. C., R. H. Wynne, and R. F. Nelson. 2003. Measuring individual tree crown diameter with Lidar and assessing its influence on estimating forest volume and biomass. Canadian Journal of Remote Sensing 29:564–577.

Potter, C., S. Klooster, R. Myneni, V. Genovese, P. N. Tan, and V. Kumar. 2003. Continental-scale comparisons of terrestrial carbon sinks estimated from satellite data and ecosystem modeling 1982–1998. Global and Planetary Change 39(3–4):201–213.

Quiñones, M. J., and D. H. Hoekman. 2004. Exploration of factors limiting Biomass estimation by polarimetric radar in tropical forests. IEEE Transactions on Geoscience and Remote Sensing 42:86–104.

Richards, P. W. 1952. The tropical rain forest. An ecological study. Cambridge University Press, Cambridge, UK.

Ryan, M. G., D. Binkley, and J. H. Fownes. 1997. Age-related decline in forest productivity: Pattern and process. Advances in Ecological Research 27:213–262.

Saatchi, S. S., R. A. Houghton, R. C. Dos Santos Alvala, J. V. Soares, and Y. Yu. 2007. Distribution of aboveground live biomass in the Amazon basin. Global Change Biology 13:816–837.

Saatchi, S. S., M. Marlier, R. L. Chazdon, D. B. Clark, and A. E. Russel. 2010. Impact of spatial variability of forest structure on radar estimation of aboveground biomass in tropical forests. Remote Sensing of Environment Special Issue, *in press*.

Sarabandi, K., and Y.-C. Lin. 2000. Simulation of Interferometric SAR response for characterizing the scattering phase center statistics of forest canopies. IEEE Transactions on Geoscience and Remote Sensing 38:115–125.

Sun, G., K. J. Ranson, D. S. Kimes, J. B. Blair, and K. Kovacs. 2008. Forest vertical structure from GLAS: An evaluation using LVIS and STRM data. Remote Sensing of Environment 112:107–117.

Thomas, R. Q., G. C. Hurtt, R. Dubayah, and M. H. Schilz. 2008. Using lidar data and a height-structured ecosystem model to estimate forest carbon stocks and fluxes over mountainous terrain. Canadian Journal of Remote Sensing 34(Supplement 2):S351–S363.

Treuhaft, R. N., B. E. Law, and G. P. Asner. 2004. Forest attributes from radar interferometric structure and its fusion with optical remote sensing. BioScience 54:561–571.

Treuhaft, R. N., and P. R. Siqueira. 2004. The calculated performance of forest structure and biomass estimates from interferometric radar. Waves in Random Media 14:S345–S358.

Whitmore, T. C. 1982. On pattern and process in forests. Pages 45–59 *in* E. I. Newman, editor. The plant community as a working mechanism. Blackwell, Oxford, UK.